nature communications

Article

https://doi.org/10.1038/s41467-026-78383-2

Colossal visible birefringence and ultraviolet hyperbolicity in wide bandgap semiconductor $CuAlO_2$

Received: 26 May 2026

Accepted: 22 September 2026

Published online: 13 October 2026

Check for updates

Baekjune Kang[1,5], Junhee Shin[1,5], Myeongjun Kang[2], Uksam Choi[1], Uihyeon Seo[1], Heekyeong Kim[3], Kunook Chung[1,3], Jong Mok Ok[2] ✉, Hosub Jin[1] ✉ & Changhee Sohn[4] ✉

Materials combining colossal birefringence with a wide bandgap are of considerable interest for miniaturized photonics, yet remain rare because strong optical transitions that enhance birefringence usually introduce optical loss. Here we show that $CuAlO_2$ exhibits colossal ultraviolet–visible birefringence alongside a wide bandgap. Spectroscopic ellipsometry on millimeter-sized single crystals reveals a sharp, intense lowest-energy transition near 3.78 eV exclusively in the ab-plane, yielding a maximum birefringence $|\Delta n|_{max} = 3.67$, and $|\Delta n| > 0.5$ throughout the visible range, with a direct band gap of 3.71 eV. The same transition generates a Type-II hyperbolic window between two ultraviolet epsilon-near-zero points. First-principles calculations and optical selection rules attribute this anisotropy to Cu-dominated band-edge states and a dipole-allowed Cu d_z^2-to-$p_{x/y}$ transition enabled by the linear O–Cu–O dumbbell structure. These results establish $CuAlO_2$ as a natural oxide platform that bridges broadband low-loss birefringence and ultraviolet hyperbolic photonics.

As photonics technologies become increasingly compact and integrated, a central materials challenge is to control light more strongly, more directionally, and with lower loss[1]. Birefringent materials are essential for this purpose, enabling polarization control, phase matching, optical modulation, and laser optics across scientific and industrial technologies[2–6]. However, conventional wide bandgap birefringent crystals, such as $LiNbO_3$, typically exhibit only modest birefringence in the visible and ultraviolet spectral ranges[7]. Recent van der Waals and low-dimensional materials have expanded the range of attainable optical anisotropy[8,9], but many rely on either intraband or low-energy interband transitions and therefore suffer from substantial absorption or limited transparency windows at shorter wavelengths[10]. This creates a persistent materials trade-off: strong optical transitions can enhance refractive-index anisotropy, but they often narrow the band gap and increase optical loss, whereas wide bandgap materials tend to show weaker anisotropy. Although metamaterials can partly overcome this limitation, scattering losses, interface disorder, and fabrication complexity remain obstacles to broad implementation[11]. Therefore, identifying natural materials that combine giant optical anisotropy with a wide bandgap remains an important challenge for broadband anisotropic photonics[12–14].

Here, we demonstrate delafossite $CuAlO_2$ as a natural oxide that overcomes the usual trade-off between large optical anisotropy and a wide bandgap. The layered lattice structure of $CuAlO_2$ contains linear O–Cu–O dumbbells that create a strongly anisotropic local bonding environment within a three-dimensionally connected oxide framework (Fig. 1a). This structural motif is crucial because it allows the c-axis optical response to be directly accessed and leveraged, rather than

[1]Department of Physics, Ulsan National Institute of Science and Technology, Ulsan, Republic of Korea. [2]Department of Physics, Pusan National University, Busan, Republic of Korea. [3]Graduate School of Semiconductor Materials and Devices Engineering, Ulsan National Institute of Science and Technology, Daejeon, Republic of Korea. [4]Department of Physics, Korea Advanced Institute of Science and Technology Daejeon, Ulsan, Republic of Korea. [5]These authors contributed equally: Baekjune Kang, Junhee Shin. ✉e-mail: okjongmok@pusan.ac.kr; hsjin@unist.ac.kr; changheesohn@kaist.ac.kr

https://doi.org/10.1038/s41467-026-78383-2

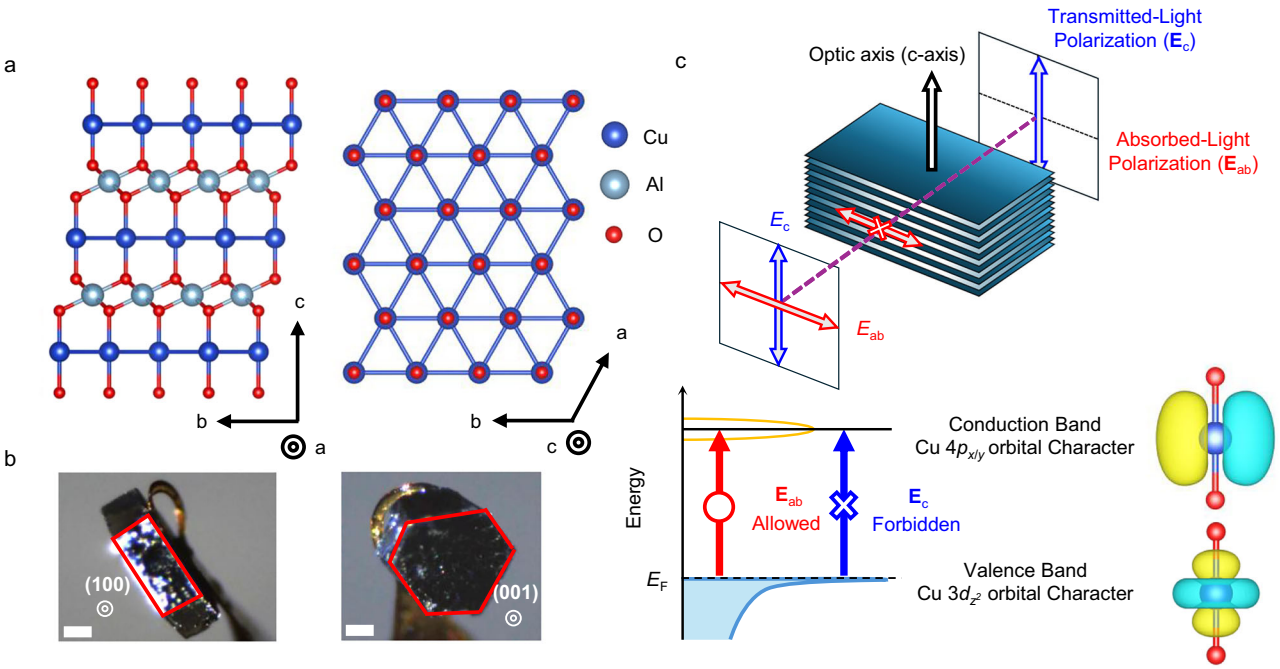

Fig. 1 | Schematics of three-dimensional crystal structure and optical anisotropy of $CuAlO_2$. **a** Schematic representation of the lattice structure of $CuAlO_2$. Blue, light blue, and red spheres indicate Cu, Al, and O atoms, respectively. **b** Microscopy images of a $CuAlO_2$ single crystal. The left panel shows the (100) side surface, while the right panel shows the (001) top surface. The red boxes indicate the corresponding surface planes. The dark appearance is attributed to the reported 1.4% Cu^{2+} defect concentration and the millimeter-scale optical path length[15]. A white bar indicates a length scale of 100 µm. **c** (Upper) Schematic illustration of the optical anisotropy of $CuAlO_2$. The red and blue arrows indicate the polarization of incident light, while the purple dashed line represents the direction of incident light propagation. The optic axis (c-axis) is shown by the black arrow. For the side facet shown in the left panel of Fig. 1b, light polarized parallel to the c-axis ($\mathbf{E}_c$) experiences weak absorption, whereas light polarized within the ab-plane ($\mathbf{E}_{ab}$) is strongly absorbed. (Lower) Schematic of the band structure and corresponding orbital character of $CuAlO_2$. The highest valence band is predominantly characterized by Cu $3d_{z^2}$, while the lowest conduction band features Cu $4p_{x/y}$ orbitals. The colossal optical anisotropy in $CuAlO_2$ is explained by the selection rules governing the transition between these orbitals and the polarization of incident light.

being limited by weak interlayer coupling as in many two-dimensional materials. Using millimeter-sized single crystals with well-defined facets (Fig. 1b), we independently determine the ab-plane and c-axis optical constants by spectroscopic ellipsometry. The key observation is that the lowest strong optical transition appears near 3.78 eV almost exclusively for the ab-plane response, while the *c*-axis response remains negligible in the same spectral range (Fig. 1c). This direction-selective transition produces a maximum birefringence of 3.67 at 333 nm, an extinction anisotropy of 5.22 at 323 nm, and $|\Delta n(\omega)| > 0.5$ throughout the entire visible range, together with a wide direct band gap of 3.71 eV. Below the bandgap, birefringence reaches 1.66 at 370 nm. At higher photon energies, the same transition drives two ultraviolet epsilon-near-zero (ENZ) points and an intervening Type-II hyperbolic window. First-principles calculations and optical selection rules reveal that the response originates from Cu-dominated band-edge states and a dipole-allowed intra-atomic-like Cu d_z^2 to $p_{x/y}$ transition enabled by the O–Cu–O dumbbell structure, providing a microscopic basis for the experimentally observed anisotropy.

Results and discussion

The anisotropic refractive indices of $CuAlO_2$ were determined by spectroscopic ellipsometry, revealing its giant optical birefringence. Using a recently reported synthesis method[15], we grew millimeter-sized $CuAlO_2$ single crystals with smooth, shiny facets (Supplementary Information). Because of the large crystal size and well-defined crystallographic faces as shown in Fig. 1b, the optical response for electric fields parallel to the ab-plane and the *c*-axis could be measured independently (Supplementary Information)[16]. Specifically, when the top surface with the c-axis normal was measured, the s-polarized electric field was parallel to the ab-plane, whereas measurements on the side surface with an in-plane surface normal allowed the s-polarized electric field to be aligned parallel to the c-axis. Under these axis-aligned geometries, the cross-polarization terms are negligible because the optic axis is either parallel or perpendicular to the s-polarized field (Supplementary Information). Therefore, the principal components of the optical tensor could be obtained directly from the direction-selective ellipsometric parameter through a model-free transformation (Supplementary Information). Fig. 2a, b show the refractive index $n(\omega)$ and extinction coefficient $k(\omega)$, respectively, for s-polarized light parallel to the ab-plane (red) and the c-axis (blue). The two responses differ markedly, indicating strong optical anisotropy. Notably, a sharp and intense optical transition appears near 3.78 eV only for light polarized parallel to the ab-plane, whereas the c-axis response remains low-loss below 5 eV. This direction-selective transition is consistent with the strong in-plane excitonic response reported in previous Bethe–Salpeter equation (BSE) calculations of $CuAlO_2$[17,18]. Through the Kramers–Kronig relation, this intense low-energy excitonic resonance strongly enhances n_{ab} below the transition, while the absence of a comparable low-energy resonance along the c-axis keeps n_c much smaller. Therefore, the polarization-dependent excitonic response is the primary origin of the large optical anisotropy in the UV–visible spectral range.

The colossal optical anisotropy and wide bandgap of $CuAlO_2$ make it attractive for photonic applications that require strong birefringence with low optical loss. Fig. 2c shows the birefringence $|\Delta n(\omega)|$ and extinction anisotropy $|\Delta k(\omega)|$ of $CuAlO_2$ at room temperature. The $|\Delta n(\omega)|$ exceeds 0.5 over nearly the entire measured spectral range, except for a narrow region at 3.86–3.9 eV immediately above the sharp optical transition. It remains above 1 over most of the range from 2.86 eV to 6.2 eV, outside this narrow interval. The maximum birefringence

https://doi.org/10.1038/s41467-026-78383-2

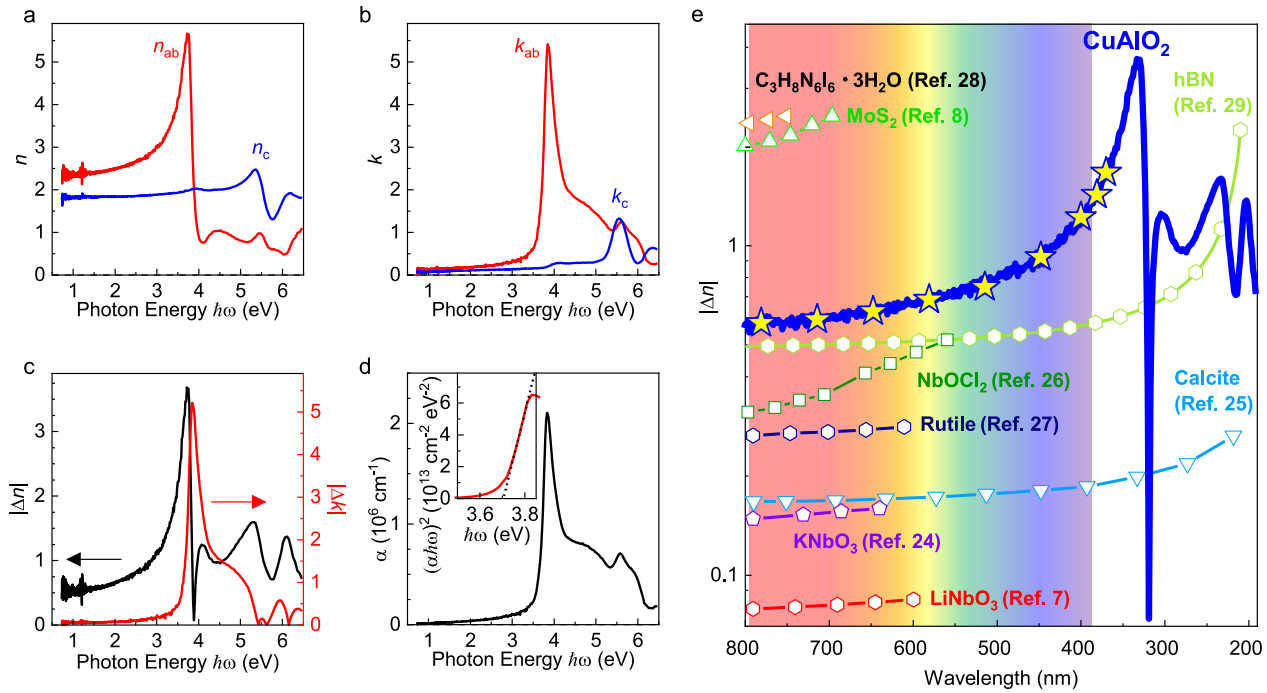

Fig. 2 | Giant optical anisotropy of $CuAlO_2$. **a** Refractive index ($n(\omega)$) and **b** extinction coefficient ($k(\omega)$) of $CuAlO_2$ at room temperature. The red and blue lines represent the ab-plane ($n_{ab}(\omega)$, $k_{ab}(\omega)$) and c-axis ($n_c(\omega)$, $k_c(\omega)$) components, respectively. **c** Absolute values of birefringence $|\Delta n(\omega)|$ and extinction anisotropy $|\Delta k(\omega)|$ of $CuAlO_2$ at room temperature. The black solid line and red open line denote $|\Delta n(\omega)|$ and $|\Delta k(\omega)|$, respectively. The maximum values of birefringence ($|\Delta n_{max}|$) and extinction anisotropy ($|\Delta k_{max}|$) are about 3.67 at 333 and 5.22 at 323 nm, respectively, which are among the largest values reported for natural anisotropic optical materials in the UV–visible range. **d** Optical absorption coefficient $\alpha(\omega)$ of $CuAlO_2$ at room temperature. Inset: direct-gap Tauc analysis. The red curve shows $(\alpha\hbar\omega)^2$, and the black line indicates the linear extrapolation of the steepest absorption-edge region used to determine the direct optical bandgap. e, Comparison of $|\Delta n(\omega)|$ between $CuAlO_2$ and representative anisotropic materials with reported band gaps above 1.55 eV, including $LiNbO_3$[7], MoS_2[8], $KNbO_3$[24], calcite[25], $NbOCl_2$[26], TiO_2[27], $C_3H_8N_6I_6 \cdot 3H_2O$[28], and hBN[29]. The symbols for the comparison materials indicate the spectral ranges used for comparison. The full measured birefringence spectrum of $CuAlO_2$ is shown, with star symbols marking selected representative data points below the indirect band gap for visual clarity. The rainbow-shaded region highlights the visible range (400–780 nm).

reaches $|\Delta n|_{max} = 3.67$ at 3.72 eV (333 nm), accompanied by a peak refractive index of $n_{ab;max} = 5.66$. The $|\Delta k(\omega)|$ is also pronounced, with $|\Delta k|_{max} = 5.22$ at 3.83 eV (323 nm), reflecting the strong polarization selectivity of the optical transition. To the best of our knowledge, these $|\Delta n|_{max}$ and $|\Delta k|_{max}$ values are among the largest reported for natural anisotropic optical materials in the UV–visible range. Figure 2d shows the absorption coefficient $\alpha(\omega)$ for the ab-plane and the corresponding optical bandgap analysis. The inset presents a direct optical bandgap Tauc analysis, in which the direct bandgap was determined from the linear region with the maximum slope, yielding a direct band gap of approximately 3.71 eV. Although the indirect-gap analysis gives a lower fundamental gap of approximately 3.45 eV (Supplementary Information), the direct-transition model is emphasized here because the UV–visible absorption edge is dominated by the optically allowed L–F transition[18–20]. Notably, this value exceeds previously reported experimental band gaps for $CuAlO_2$ but closely matches the value predicted by recent hybrid-functional pseudopotential calculations[18,21]. This difference in experimental band gaps is likely associated with the experimental method used to determine the absorption coefficient. Previous transmission-based analyses may have relied on apparent absorption coefficients without fully accounting for surface reflection and scattering losses, whereas the present Tauc analysis uses the absorption coefficient calculated directly from the ellipsometry-derived optical constants[21,22]. The sub-gap absorption below the direct band edge is likely associated with the reported ~1.4% Cu^{2+} defect concentration and can lead to strong apparent darkening in millimeter-thick crystals (Supplementary Information)[15,23]. At 1 eV, the present crystal shows finite extinction coefficients of $k_{ab} \sim 0.12$ and $k_c \sim 0.07$, reflecting the sub-gap absorption background. Further reduction of Cu^{2+}-related defects and other sub-gap absorption sources will therefore be important for improving the practical optical performance of $CuAlO_2$.

The optical response of $CuAlO_2$ is further evaluated by benchmarking its birefringence against other UV–visible low-loss anisotropic materials. Fig. 2e compares the $|\Delta n(\omega)|$ of $CuAlO_2$ within its low-loss spectral range with representative anisotropic optical materials, including rutile and $LiNbO_3$, and other recently reported birefringent crystals[7,8,24–29]. For a comparison relevant to UV–visible photonics, we selected materials with reported band gaps above approximately 1.55 eV, corresponding to a photon wavelength of approximately 800 nm. For example, while the solution-processable natural crystal exhibits large birefringence, its relatively small band gap and strong visible absorption restrict its practical lower-loss operation to a limited spectral range[28]. As shown in Fig. 2e, conventional optical crystals that remain transparent across the visible range generally exhibit modest birefringence. By contrast, many materials with larger birefringence show strong optical loss in the visible or near-UV region, limiting their lower-loss operation to the near-infrared or a restricted visible window. $CuAlO_2$ overcomes this trade-off by maintaining a lower-loss optical window across the visible range while exhibiting larger $|\Delta n(\omega)|$ than other anisotropic materials. $CuAlO_2$ maintains a large $|\Delta n(\omega)|$ exceeding 0.5 throughout this lower-loss spectral region. In particular, $CuAlO_2$ reaches $|\Delta n(\omega)| = 1.66$ at 370 nm, which, to the best of our knowledge, represents the largest value among the UV–visible lower-loss anisotropic materials surveyed here. $CuAlO_2$ also exhibits larger birefringence than recently reported hexagonal boron nitride (hBN) across the entire visible spectral range[29]. This combination of broadband low-loss and large birefringence distinguishes $CuAlO_2$ from both conventional optical crystals and recently discovered high-anisotropy

https://doi.org/10.1038/s41467-026-78383-2

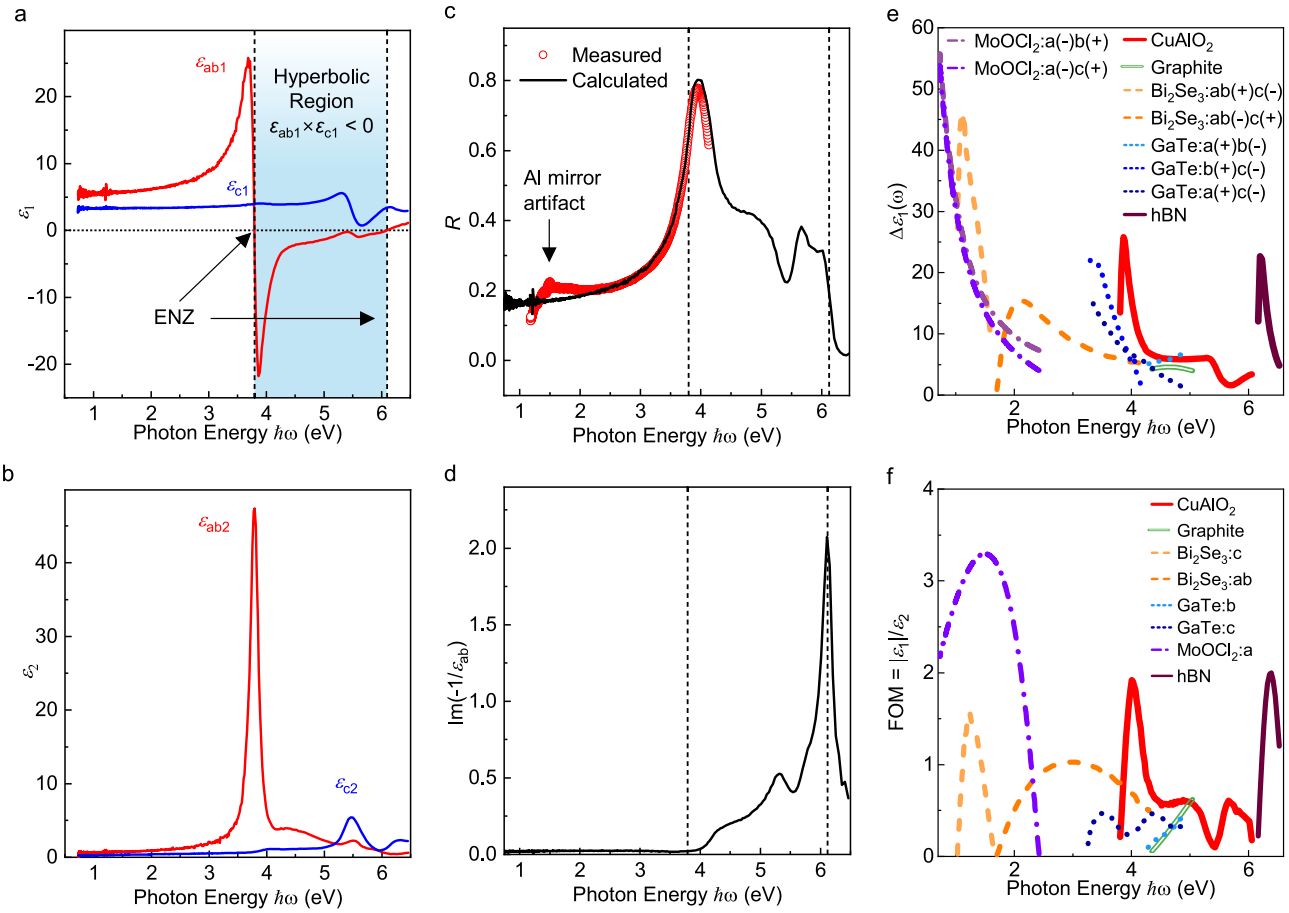

Fig. 3 | The hyperbolic region in $CuAlO_2$. **a** Real part and **b** imaginary part of the dielectric function of $CuAlO_2$ at room temperature. The red and blue lines correspond to the in-plane ($\varepsilon_{ab1}(\omega)$, $\varepsilon_{ab2}(\omega)$) and out-of-plane ($\varepsilon_{c1}(\omega)$, $\varepsilon_{c2}(\omega)$) components, respectively. The horizontal dashed line marks $\varepsilon_1 = 0$, and its intersections with ε_{ab1} define the two epsilon-near-zero (ENZ) points. The light blue shaded region highlights the hyperbolic region, where the signs of the anisotropic dielectric tensor components differ. **c** Normal incidence reflectance spectrum from the c-axis surface. Red open circles and the black solid line represent the measured and calculated reflectance spectra, respectively. The weak feature near 1.5 eV originates from an Al-mirror reference artifact. **d** Calculated energy-loss function Im(−1/ε_{ab}). The vertical dashed lines in **c** and **d** indicate the ENZ energies that bound the negative ε_{ab1} region. The Reststrahlen-like high-reflectance band in **c** and the longitudinal loss-function peak in **d** provide spectroscopic support for the optically metallic in-plane response associated with ε_{ab1}. **e** Dielectric anisotropy $\Delta\varepsilon(\omega) = |\varepsilon_{ab1}(\omega) - \varepsilon_{c1}(\omega)|$ and **f** hyperbolic figure of merit (FOM), $|\varepsilon_1|/\varepsilon_2$, for various hyperbolic materials, $MoOCl_2$[9], hBN[29], Bi_2Se_3[33], Bi_2Te_3[33], graphite[34], and GaTe[35,36]. $CuAlO_2$ is shown as a red solid line, whereas the comparison materials are distinguished by different line styles.

materials, positioning it as a natural oxide platform for UV–visible polarization optics.

While the sub-bandgap spectral range highlights the giant birefringence of $CuAlO_2$, the higher-energy region above the optical transition reveals an additional optical functionality arising from the direction-selective response. In particular, the strong polarization-dependent dispersion of the dielectric tensor produces ultraviolet ENZ points and an intervening Type-II hyperbolic regime. The ENZ condition is useful because a near-zero principal dielectric component can strongly modify phase accumulation and enhance the electric-field component along the ENZ axis, providing a route toward field concentration and enhanced light–matter interaction[30]. In the hyperbolic regime, the opposite signs of the principal dielectric components open the optical momentum space, allowing access to high-q states that are normally evanescent in conventional dielectrics and increasing the photonic density of states[31]. Such UV-accessible ENZ and hyperbolic responses remain uncommon in natural materials, and this spectral range has been far less explored than the infrared or visible regimes. Establishing low-loss, strongly anisotropic natural materials in the UV is therefore an important step toward extending ENZ and hyperbolic optical functionalities to shorter wavelengths[32].

In $CuAlO_2$, the sharp direction-selective excitonic optical transition not only enhances birefringence but also reverses the sign of the in-plane dielectric response, producing two ENZ points that bound a broad UV Type-II hyperbolic window. Fig. 3a, b show the real and imaginary parts of the principal dielectric functions, $\varepsilon_{ab}(\omega)$ and $\varepsilon_c(\omega)$, extracted parallel to the ab-plane and the c-axis, respectively. The sharp and intense absorption peak near 3.78 eV for ab-plane response, together with the weak c-axis absorption in the same energy range, produces a large dispersive change in ε_{ab1}. This strong dispersion drives ε_{ab1} through zero at two ENZ points, one near 3.8 eV and the other near 6.2 eV. Within this interval, ε_{ab1} remains negative while ε_{c1} remains positive, giving rise to a Type-II hyperbolic regime, $\varepsilon_{ab1} \times \varepsilon_{c1} < 0$, across the intervening UV spectral window (Supplementary Information)[31].

To further verify the optically metallic in-plane response underlying the UV hyperbolic region, we compared the measured normal-incidence reflectance with the calculated reflectance and evaluated the corresponding energy-loss spectrum from the ellipsometry-derived in-plane dielectric function. As shown in Fig. 3c, the measured ab-plane reflectance exhibits a high-reflectance band in the same spectral region where ε_{ab1} becomes negative, and this feature is consistent with the calculated reflectance. This agreement confirms that the high-

reflectance band originates from the intrinsic in-plane dielectric response of $CuAlO_2$ (Supplementary Information). Fig. 3d shows the calculated energy-loss spectrum, $\mathrm{Im}(-1/\varepsilon_{ab})$, which represents the longitudinal dielectric response. The strong in-plane optical transition at the lower-energy side acts as a transverse interband resonance, whereas the sharp loss-function maximum near the upper-energy ENZ point corresponds to a longitudinal excitation. Therefore, the high-reflectance band observed in both the measured and calculated spectra, together with the calculated longitudinal loss peak, corroborates the assignment of the negative-ε_{ab1} region as a Reststrahlen-like optically metallic band[29].

$CuAlO_2$ exhibits a UV hyperbolic response by combining a broad Type-II hyperbolic window with a hyperbolic figure of merit. Fig. 3e compares the dielectric anisotropy $\Delta\varepsilon_1(\omega) = |\varepsilon_{ab1}(\omega) - \varepsilon_{c1}(\omega)|$ of $CuAlO_2$ with representative natural hyperbolic materials whose anisotropic optical responses extend into the UV spectral range[9,29,33–36]. Within the overlapping UV spectral range where hyperbolicity has been reported, $CuAlO_2$ shows the largest $\Delta\varepsilon_1$ among the natural materials surveyed here. A similar advantage is observed in the hyperbolic figure of merit, $\mathrm{FOM} = |\varepsilon_1|/\varepsilon_2$, shown in Fig. 3f. $CuAlO_2$ reaches FOM = 1.91 at 4.01 eV and remains comparatively high over the UV hyperbolic window, indicating a balance between dielectric anisotropy and optical loss. For comparison, recently reported hBN reaches FOM = 2.00 at 6.39 eV in the deep-UV region[29], whereas $MoOCl_2$ reaches FOM = 3.29 at 1.5 eV in the visible region[9]. These comparisons highlight the distinct role of $CuAlO_2$ as a natural hyperbolic oxide operating in the UV spectral window between visible-frequency $MoOCl_2$ and deep-UV hBN, while maintaining one of the largest dielectric anisotropies among the surveyed UV hyperbolic materials. Together, these results establish $CuAlO_2$ as a rare natural oxide in which large visible birefringence and UV-accessible ENZ/Type-II hyperbolicity coexist, enabling anisotropic optical functionality across a broad visible-to-ultraviolet spectral range.

The origin of the direction-selective optical response in $CuAlO_2$ can be understood from its lattice symmetry and orbital character near the band edge. Previous theoretical studies have identified quasi-two-dimensional optical transitions in $CuAlO_2$, suggesting that this behavior likely arises from its layered structure[17,18]. However, the microscopic orbital origin of this strongly polarization-dependent transition has not been fully clarified. To address this point, we performed ab initio calculations using the generalized gradient approximation (GGA) method. Although GGA does not accurately reproduce the absolute bandgap and quantitative optical spectral weight, it is sufficient for identifying the orbital characters and symmetry-derived selection rules relevant to the anisotropic optical response. This use is further supported by previous self-consistent GW calculations, which showed that the wavefunction character near the L point, where the primary optical transition occurs, is only weakly modified apart from the band gap correction[37]. Moreover, recent hybrid-functional pseudopotential calculations and GW–BSE have quantitatively reproduced the optical properties of $CuAlO_2$ in close agreement with our experimental spectra[18,19]. Therefore, we use GGA-level wavefunctions to clarify the qualitative orbital and symmetry origin of the experimentally observed anisotropic transition, rather than attempting to reproduce the optical spectrum quantitatively.

The anisotropic optical transition in $CuAlO_2$ originates from the orbital character imposed by the linear O–Cu–O dumbbell structure. Fig. 4a shows the calculated band structure and partial density of states (PDOS) of $CuAlO_2$, which are qualitatively consistent with previous reports[18,38]. The electronic states near the band edges are mainly composed of Cu and O orbitals, with negligible contribution from Al orbitals. To resolve the orbital contributions in more detail, we present the orbital-projected band structure and PDOS with Cu 3*d* orbitals (Fig. 4b), Cu 4*p* orbitals (Fig. 4c), and O 2*p* orbitals (Fig. 4d). The upper valence band is dominated by Cu d_z^2 character with a moderate O p_z contribution, whereas the lowest optically active conduction states along the L–F line contain strong Cu $p_{x/y}$ character and a minor O $p_{x/y}$ contribution (Supplementary Information). As indicated by a black arrow and red box in Fig. 4a, the primary optical transition occurs near this region of the Brillouin zone[18–20]. Importantly, the Cu d_z^2 character is strongly suppressed in the conduction band along this transition pathway, while Cu $p_{x/y}$ orbitals dominate. This separation of Cu 3*d* and 4*p* orbital characters is consistent with the symmetry constraint of the linear O–Cu–O dumbbell structure, which suppresses intra-atomic *d*-*p* orbital mixing[40]. Furthermore, the dumbbell structure pushes the Cu p_z orbital to higher energy relative to the Cu $p_{x/y}$ orbitals. As a result, the transition from the Cu d_z^2 + O p_z states to the Cu $p_{x/y}$ + O $p_{x/y}$ states is optically allowed.

We confirm that the dominant lowest-energy optically allowed transition occurs from Cu d_z^2 to Cu $p_{x/y}$, as verified by the Bloch functions of electron and hole states (Fig. 4e). The valence-band Bloch function is dominated by Cu d_z^2 with a minor O p_z contribution directed toward the Cu atom. In contrast, the conduction-band Bloch function primarily consists of Cu $p_{x/y}$ with a minor O $p_{x/y}$ contribution extending toward the Al atom. This spatial arrangement further supports the intra-atomic-like nature of the transition: the O $p_{x/y}$ component in the conduction state has only weak spatial overlap with the Cu-centered d_z^2 valence state, making an intersite O-Cu transition unlikely to dominate the optical response. Consistently, the dielectric function calculated from the electronic structure shows that the lowest-energy optical transition is concentrated along the L–F line and is allowed only for ab-plane-polarized light (Supplementary Information). According to the dipole selection rule, the transition from Cu d_z^2 to Cu $p_{x/y}$ is allowed for light polarized in the ab-plane, whereas the corresponding transition is forbidden for light polarized along the c-axis[41]. Because this transition is largely localized on the Cu site, its transition probability can be high, giving rise to the intense in-plane optical absorption observed near 3.78 eV[17]. Therefore, the linear O–Cu–O dumbbell structure, the Cu-dominated orbital character near the band edge, and the resulting dipole selection rule provide a microscopic origin for the giant optical anisotropy observed experimentally in $CuAlO_2$.

In summary, we have established $CuAlO_2$ as a natural oxide with giant UV–visible optical anisotropy by independently determining its principal optical constants along the ab-plane and c-axis. The direction-selective in-plane optical transition produces colossal birefringence over the visible–UV spectral range and drives two ENZ crossings that bound a UV Type-II hyperbolic window. Combined with its wide direct band gap and low optical loss, this response distinguishes $CuAlO_2$ from conventional birefringent crystals and recently explored natural hyperbolic materials. First-principles calculations further show that the giant anisotropy originates from the Cu-dominated band-edge states and the dipole-allowed intra-atomic-like Cu d_z^2-to-$p_{x/y}$ transition enabled by the linear O–Cu–O dumbbell structure.

The large $|\Delta n(\omega)|$ between the ab-plane and c-axis responses of $CuAlO_2$ also provides an important degree of freedom for polarization optics. Unlike many layered anisotropic materials, where the out-of-plane optical response is tied to a weakly bonded interlayer direction and can be difficult to exploit in device geometries, $CuAlO_2$ is a three-dimensionally connected non-van der Waals oxide. This structural character makes the c-axis optical response potentially accessible through crystal orientation, facet engineering, and non-basal-oriented thin films[42]. Translating these properties into practical photonic components will require future efforts in oriented thin-film growth[43,44] and device-level demonstrations[45] that exploit both the in-plane and out-of-plane optical axes. This structural advantage points toward compact UV–visible polarization optics, such as thin phase retarders and waveplates[46]. Additionally, the UV Type-II hyperbolic response of $CuAlO_2$ is significant because extending natural hyperbolic media to shorter wavelengths directly enables access to smaller photonic length

https://doi.org/10.1038/s41467-026-78383-2

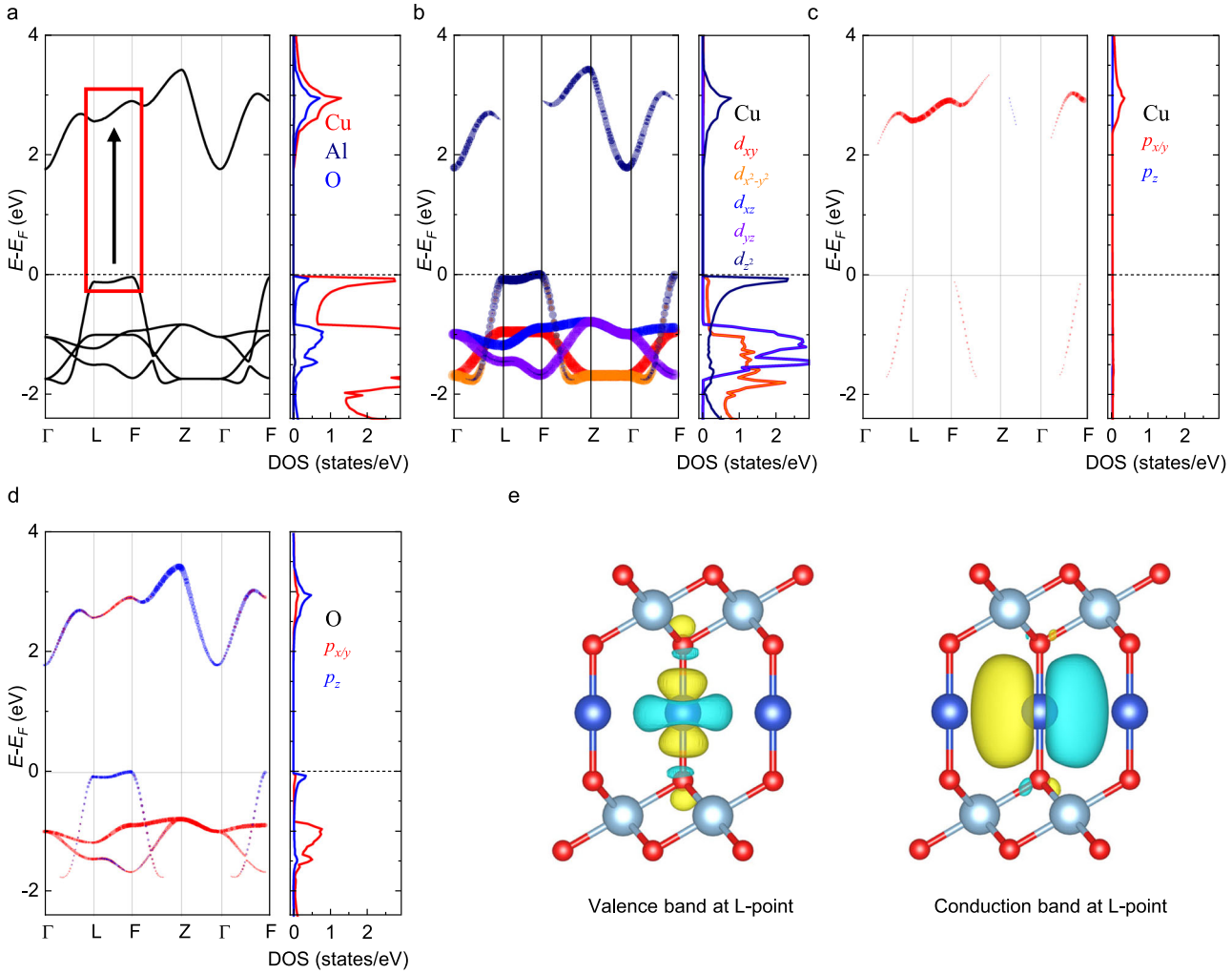

Fig. 4 | Electronic structure and orbital origin of optical anisotropy in $CuAlO_2$. **a** Band structure and atom-selective partial density of states (PDOS) of $CuAlO_2$ near the Fermi level. The band structure is plotted along the high-symmetry path in the rhombohedral Brillouin zone. Only Cu and O atoms contribute to the band near the Fermi level. The orbital-projected band structures and PDOS of $CuAlO_2$ are represented by **b** Cu *d* orbitals, **c** Cu *p* orbitals, and **d** O *p* orbitals. The color coding for the orbital symmetries is defined in the key within each panel, while the symbol size represents the relative orbital contribution. **e** Real-space projected Bloch functions for the highest valence band and lowest conduction band at the L point. Blue, light-blue, and red spheres represent Cu, Al, and O atoms, respectively, consistent with Fig. 1a. Yellow and cyan isosurfaces indicate opposite signs of the Bloch wave-functions. Both functions are predominantly localized within the Cu layers, consistent with the quasi-two-dimensional character of the electronic states.

scales and larger optical momenta. Such UV hyperbolic responses are relevant for high-*q* optical-state engineering[47], enhanced light–matter interaction[48], super-resolution imaging[49], and high-resolution photolithography[50]. For example, its UV hyperbolic window overlaps with the KrF excimer-laser wavelength of 248 nm, making photolithography-related UV optical-state engineering one possible application direction. Direct near-field imaging or momentum-resolved measurements of UV hyperbolic polariton propagation would be an important future step toward validating and exploiting these nanoscale photonic functionalities. These findings position $CuAlO_2$ as a natural oxide platform bridging broadband birefringent optics and ultraviolet anisotropic nanophotonics.

Methods

Sample preparation and characterization

$CuAlO_2$ single crystals were grown by the reactive crucible melting method[15]. Cu_2O powder (2.5 g) was placed in an alumina crucible (99.9% purity) and heated to 1225 °C for 6 h. Following the holding process, the furnace was cooled to 1150 °C at a rate of 1 °C per hour and then cooled to room temperature. Several crystals formed within the crucible, and individual single crystals were mechanically separated. The resulting crystals were 1–2 mm long and appeared as black, shiny hexagonal pillars. The crystal structure was confirmed by single-crystal X-ray diffraction. The measurements were performed on a D8 Venture (Bruker) using a Mo Kα X-ray source. The crystal structure was determined by refinement using the built-in software (APEX 4).

Raman spectra were acquired at 300 K using an unpolarized 532 nm laser and a charge-coupled device (CCD; DU401A, Andor Technology) coupled to a monochromator (Omni-λ2002i, Zolix). The acquisition time was 20 s per spectrum.

Ellipsometry, Mueller Matrix, reflectance, and optical constants of $CuAlO_2$

The optical properties of $CuAlO_2$ were obtained using an M-2000 ellipsometer (J. A. Woollam Co.). All samples were mounted with silver epoxy onto oxygen-free copper cones to suppress backside reflections. The ellipsometry parameters, Ψ (the amplitude ratio of reflected p- and s-polarized light) and Δ (the phase difference of reflected p- and s-polarized light), of $CuAlO_2$ were measured over the energy range of 0.74–6.46 eV (5900–52000 cm^{-1}) at an angle of incidence $\theta = 70°$.

Owing to the size and thickness of the $CuAlO_2$ single crystals, the top surface, with its normal parallel to the c-axis, and a shiny side facet, with its normal perpendicular to the c-axis, were measured independently. In both geometries, the optic axis is aligned either parallel or perpendicular to the s-polarization, thereby suppressing cross-polarization mixing. Consequently, the measured ellipsometric response is dominated by the dielectric-function component parallel to the s-polarized electric field[16]. Although the orthogonal refractive-index component is formally present, the measurement geometry is only weakly sensitive to this component, allowing its contribution to be neglected[8]. The complex dielectric functions were obtained from the measured ellipsometric parameters using

$$\varepsilon_1 + i\varepsilon_2 = \sin^2\theta\left[1 + \tan^2\theta(1-\rho/1+\rho)^2\right], \quad (1)$$

where $\rho = \tan(\Psi)e^{i\Delta}$. Other optical constants were calculated from the extracted dielectric function.

To validate this assumption and the absence of appreciable cross-polarization mixing, additional measurements were also performed in the Mueller-matrix acquisition mode of the M-2000. We compared the Mueller-matrix response of the $CuAlO_2$ (001) surface with that of a non-axis-aligned $CuAlO_2$ facet whose exact Miller index was not determined (Supplementary Information).

The reflectance spectra of $CuAlO_2$ were measured to independently compare the optical response with the dielectric functions extracted from spectroscopic ellipsometry. Measurements were performed using a 20/20 PV UV−Vis microspectrometer (CRAIC Technologies) under near-normal-incidence conditions with unpolarized light at 300 K. The spectra were acquired from the top surface of the crystal, whose surface normal is parallel to the c-axis. Under near-normal incidence, the electric field lies predominantly within the ab-plane; therefore, the unpolarized reflectance primarily probes the in-plane optical response, simplifying the analysis. The measurement procedure consisted of three sequential steps: (i) recording the dark background, (ii) acquiring the reflectance spectrum of an aluminum mirror reference, and (iii) measuring the reflectance spectrum of the $CuAlO_2$ sample. The final reflectance was obtained by subtracting the dark background from both the sample and reference spectra and then taking the ratio of the corrected $CuAlO_2$ intensity to the corrected aluminum mirror intensity. All measurements were performed using the microscope attachment of the spectrometer with a probed area of approximately 40 × 40 µm. Each spectrum was acquired with an integration time of 11 ms, and 60 spectra were averaged to obtain the final dataset. The spectral range was 300–1050 nm with a spectral resolution of 0.5 nm.

Electronic structure calculations

Density functional theory calculations were performed using the projector-augmented wave method as implemented in the Vienna Ab-initio Simulation Package (VASP)[51,52]. The PAW potentials were generated using the following valence-electron configurations: Cu $3p^6\ 3d^{10}\ 4s^1$, Al $3s^2\ 3p^1$, and O $2s^2\ 2p^4$. The exchange-correlation functional was described as the GGA of the Perdew-Burke-Ernzerhof[53]. The plane-wave cutoff energy was 700 eV, and the first Brillouin zone was sampled with an 11 × 11 × 11 Monkhorst−Pack **k**-point grid[54]. The energy convergence for the self-consistent field approach was set to 10^{-6} eV. The plane-wave cutoff energy and **k**-point grid were sufficient to converge the total energy within 1 meV per atom. Structural optimization continued until the forces on each atom were reduced to less than 0.002 eV $Å^{-1}$. To calculate the dielectric function, a Wannier-interpolated tight-binding Hamiltonian was constructed using the Wannier90 code based on the Cu 3*d*, 4*s*, and 4*p*, Al 3*s* and 3*p*, and O 2*p* orbitals[55,56]. The dielectric function was calculated using the tight-binding model with a 250 × 250 × 250 **k**-mesh.

Data availability

The source data deposited for this study are available in Figshare at https://doi.org/10.6084/m9.figshare.33472276. All other data that support the findings of this study are available from the corresponding authors upon request.

References

1. Ko, J. H., Yoo, Y. J., Lee, Y., Jeong, H.-H. & Song, Y. M. A review of tunable photonics: optically active materials and applications from visible to terahertz. *IScience* **25**, 104727 (2022).
2. Weber, M. F., Stover, C. A., Gilbert, L. R., Nevitt, T. J. & Ouderkirk, A. J. Giant birefringent optics in multilayer polymer mirrors. *Science* **287**, 2451–2456 (2000).
3. Chen, X. et al. Solution-processed inorganic perovskite crystals as achromatic quarter-wave plates. *Nat. Photonics* **15**, 813–816 (2021).
4. Dorohoi, D. O. et al. Review on optical methods used to characterize the linear birefringence of polymer materials for various applications. *Molecules* **28**, 2955 (2023).
5. Tudi, A., Han, S., Yang, Z. & Pan, S. Potential optical functional crystals with large birefringence: recent advances and future prospects. *Coord. Chem. Rev.* **459**, 214380 (2022).
6. Jung, G. Y., Ren, G., Omprakash, P., Ravichandran, J. & Mishra, R. Design principles and identification of birefringent materials. *Chem. Mater.* **37**, 5796–5804 (2025).
7. Zelmon, D. E., Small, D. L. & Jundt, D. Infrared corrected Sellmeier coefficients for congruently grown lithium niobate and 5 mol.% magnesium oxide–doped lithium niobate. *JOSA B.* **14**, 3319–3322 (1997).
8. Ermolaev, G. et al. Giant optical anisotropy in transition metal dichalcogenides for next-generation photonics. *Nat. Commun.* **12**, 854 (2021).
9. Ermolaev, G. et al. Giant optical anisotropy and visible-frequency epsilon-near-zero in hyperbolic van der Waals $MoOCl_2$. *Nano Lett.* **26**, 4329–4338 (2026).
10. Munkhbat, B., Wróbel, P., Antosiewicz, T. J. & Shegai, T. O. Optical constants of several multilayer transition metal dichalcogenides measured by spectroscopic ellipsometry in the 300–1700 nm range: high index, anisotropy, and hyperbolicity. *ACS Photonics* **9**, 2398–2407 (2022).
11. Kats, M. A. et al. Giant birefringence in optical antenna arrays with widely tailorable optical anisotropy. *Proc. Natl. Acad. Sci.* **109**, 12364–12368 (2012).
12. Mei, H. et al. Colossal optical anisotropy from atomic-scale modulations. *Adv. Mater.* **35**, 2303588 (2023).
13. Niu, S. et al. Giant optical anisotropy in a quasi-one-dimensional crystal. *Nat. Photonics* **12**, 392–396 (2018).
14. Slavich, A. S. et al. Exploring van der Waals materials with high anisotropy: geometrical and optical approaches. *Light.: Sci. Appl.* **13**, 68 (2024).
15. Kim, D. H. et al. Growth of delafossite $CuAlO_2$ single crystals in a reactive crucible. *J. Phys.: Condens. Matter* **35**, 024002 (2022).
16. Fujiwara, H. *Spectroscopic Ellipsometry: Principles and Applications*. (John Wiley & Sons, 2007).
17. Laskowski, R., Christensen, N. E., Blaha, P. & Palanivel, B. Strong excitonic effects in $CuAlO_2$ delafossite transparent conductive oxides. *Phys. Rev. B—Condens. Matter Mater. Phys.* **79**, 165209 (2009).
18. Shen, J., Liu, H. & Li, Y. On the bandgap underestimation of delafossite transparent conductive oxides $CuMO_2$ (M = Al, Ga and In): role of pseudopotentials. *J. Chem. Phys.* **159**, 014706 (2023).
19. Wang, X., Meng, W. & Yan, Y. Electronic band structures and excitonic properties of delafossites: a GW-BSE study. *J. Appl. Phys.* **122**, 085104 (2017).

20. Nie, X., Wei, S.-H. & Zhang, S. Bipolar doping and band-gap anomalies in delafossite transparent conductive oxides. *Phys. Rev. Lett.* **88**, 066405 (2002).
21. Pellicer-Porres, J. et al. On the band gap of $CuAlO_2$ delafossite. *Appl. Phys. Lett.* **88**, 181904 (2006).
22. Klein, J. et al. Limitations of the Tauc plot method. *Adv. Funct. Mater.* **33**, 2304523 (2023).
23. Urbach, F. The long-wavelength edge of photographic sensitivity and of the electronic absorption of solids. *Phys. Rev.* **92**, 1324 (1953).
24. Zysset, B., Biaggio, I. & Günter, P. Refractive indices of orthorhombic $KNbO_3$. I. Dispersion and temperature dependence. *JOSA B.* **9**, 380–386 (1992).
25. Ghosh, G. Dispersion-equation coefficients for the refractive index and birefringence of calcite and quartz crystals. *Opt. Commun.* **163**, 95–102 (1999).
26. Guo, Q. et al. Colossal in-plane optical anisotropy in a two-dimensional van der Waals crystal. *Nat. Photonics* **18**, 1170–1175 (2024).
27. Jellison, G. E., Cureton, W. F. & Arteaga, O. Optical functions of uniaxial rutile and anatase (TiO_2) revisited. *Surf. Sci. Spectra* **31**, 026001 (2024).
28. Zhou, Y. et al. A solution-processable natural crystal with giant optical anisotropy for efficient manipulation of light polarization. *Nat. Photonics* **18**, 922–927 (2024).
29. Choi, B. et al. Natural hyperbolicity of hexagonal boron nitride in the deep ultraviolet. *Nat. Commun.* **17**, 2869 (2026).
30. Reshef, O., De Leon, I., Alam, M. Z. & Boyd, R. W. Nonlinear optical effects in epsilon-near-zero media. *Nat. Rev. Mater.* **4**, 535–551 (2019).
31. Narimanov, E. E. & Kildishev, A. V. Naturally hyperbolic. *Nat. Photonics* **9**, 214–216 (2015).
32. Sun, J., Litchinitser, N. M. & Zhou, J. Indefinite by nature: from ultraviolet to terahertz. *Acs Photonics* **1**, 293–303 (2014).
33. Esslinger, M. et al. Tetradymites as natural hyperbolic materials for the near-infrared to visible. *Acs Photonics* **1**, 1285–1289 (2014).
34. Sun, J., Zhou, J., Li, B. & Kang, F. Indefinite permittivity and negative refraction in natural material: Graphite. *Appl. Phys. Lett.* **98**, 101901 (2011).
35. Korzeb, K., Gajc, M. & Pawlak, D. A. Compendium of natural hyperbolic materials. *Opt. express* **23**, 25406–25424 (2015).
36. Palik, E. D. & Gosh, G. *The Electronic Handbook of Optical Constants of Solids*. (Academic Press, 1999).
37. Trani, F., Vidal, J., Botti, S. & Marques, M. A. Band structures of delafossite transparent conductive oxides from a self-consistent GW approach. *Phys. Rev. B-Condens. Matter Mater. Phys.* **82**, 085115 (2010).
38. Gillen, R. & Robertson, J. Band structure calculations of $CuAlO_2$, $CuGaO_2$, $CuInO_2$, and $CuCrO_2$ by screened exchange. *Phys. Rev. B-Condens. Matter Mater. Phys.* **84**, 035125 (2011).
39. Aston, D. et al. High-resolution x-ray spectroscopic study of the electronic structure of the prototypical p-type transparent conducting oxide $CuAlO_2$. *Phys. Rev. B.—Condens. Matter Mater. Phys.* **72**, 195115 (2005).
40. Orgel, L. 843. Stereochemistry of metals of the B sub-groups. Part I. Ions with filled d-electron shells. *J. Chem. Soc. (Resume.)* **161**, 4186–4190 (1958).
41. Dresselhaus, M. S., Dresselhaus, G. & Jorio, A. *Group Theory: Application to the Physics of Condensed Matter*. (Springer Science & Business Media, 2007).
42. Hoang, D. V. et al. Optical-thermoelectric trade-off in Mg-doped $CuCrO_2$ films via crystal orientation control with an oxygen-rich seed layer. *Cryst. Growth Des.* **25**, 6486–6491 (2025).
43. Kim, S.-Y., Lee, J.-H., Kim, J.-J. & Heo, Y.-W. Preferential growth orientations of $CuCrO_2$ films grown by pulsed laser deposition. *Curr. Appl. Phys.* **12**, S123–S126 (2012).
44. Van Hoang, D. et al. Fine-tuning high electrical conductivity of Mg-Doped $CuCrO_2$ delafossite thin films through preferred-(110) orientation and film thickness control. *Phys. B: Condens. Matter* **667**, 415185 (2023).
45. Lynch, J. et al. Gate-tunable optical anisotropy in wafer-scale, aligned carbon nanotube films. *Nat. Photonics* **18**, 1176–1184 (2024).
46. Melchioni, N. et al. Giant optical anisotropy in a natural van der Waals hyperbolic crystal for visible light low-loss polarization control. *ACSN nano* **19**, 25413–25421 (2025).
47. Ermolaev, G. et al. Van der Waals materials for subdiffractional light guidance. *Photonics* **9**, 744 (2022).
48. Caspani, L. et al. Integrated sources of photon quantum states based on nonlinear optics. *Light.: Sci. Appl.* **6**, e17100–e17100 (2017).
49. Liu, Z., Lee, H., Xiong, Y., Sun, C. & Zhang, X. Far-field optical hyperlens magnifying sub-diffraction-limited objects. *science* **315**, 1686–1686 (2007).
50. Sun, J. & Litchinitser, N. M. Toward practical, subwavelength, visible-light photolithography with hyperlens. *ACS Nano* **12**, 542–548 (2018).
51. Kresse, G. & Furthmüller, J. Efficient iterative schemes for ab initio total-energy calculations using a plane-wave basis set. *Phys. Rev. B.* **54**, 11169 (1996).
52. Blöchl, P. E. Projector augmented-wave method. *Phys. Rev. B.* **50**, 17953 (1994).
53. Perdew, J. P., Burke, K. & Ernzerhof, M. Generalized gradient approximation made simple. *Phys. Rev. Lett.* **77**, 3865 (1996).
54. Monkhorst, H. J. & Pack, J. D. Special points for Brillouin-zone integrations. *Phys. Rev. B.* **13**, 5188 (1976).
55. Mostofi, A. A. et al. wannier90: a tool for obtaining maximally-localised Wannier functions. *Comput. Phys. Commun.* **178**, 685–699 (2008).
56. Marzari, N. & Vanderbilt, D. Maximally localized generalized Wannier functions for composite energy bands. *Phys. Rev. B.* **56**, 12847 (1997).

Acknowledgments

The M-2000 ellipsometer (J. A. Woollam Co.) used for optical measurements was supported by the IBS Center for Correlated Electron Systems, Seoul National University.

Author contributions

B.K., J.M.O., H.J., and C.S. conceptualized this work. M.K. and J.M.O. synthesized and characterized the single crystals. B.K. and C.S. performed spectroscopic ellipsometry and reflectance measurements. B.K., H.K., K.C., and C.S. performed Raman spectroscopy. J.S. and H.J. conducted the first-principles calculations. B.K., J.S., M.K., U.C., U.S., H.K., K.C., J.M.O., H.J., and C.S. analyzed the data. B.K. and C.S. wrote the paper with input from all coauthors.

Funding

This research was supported by the National R&D Program through the National Research Foundation of Korea (NRF), funded by the Ministry of Science and ICT (2022M3H4A1A04096465, RS-2024-00348920, RS-2025-02272971, 2023R1A2C1007634, RS-2023-NR076899, RS-2026-25520808, RS-2023-00210295, RS-2021-NR060087, and RS-2026-25492893). This research was supported by the Korea Basic Science Institute (National Research Facilities and Equipment Center) grant funded by the Ministry of Education (No. RS-2024-00435344). This work was supported by the IITP (Institute of Information & Communications Technology Planning & Evaluation)-ITRC(Information Technology

Research Center) grant funded by the Korea government (Ministry of Science and ICT) (RS-2023-00259676).

Competing interests
The authors declare no competing interests.

Additional information
Supplementary information The online version contains supplementary material available at https://doi.org/10.1038/s41467-026-78383-2.

Correspondence and requests for materials should be addressed to Jong Mok Ok, Hosub Jin or Changhee Sohn.

Peer review information *Nature Communications* thanks Qiangbing Guo, Sangen Zhao and the other anonymous reviewer(s) for their contribution to the peer review of this work. A peer review file is available.

Reprints and permissions information is available at http://www.nature.com/reprints

Publisher's note Springer Nature remains neutral with regard to jurisdictional claims in published maps and institutional affiliations.

Open Access This article is licensed under a Creative Commons Attribution-NonCommercial-NoDerivatives 4.0 International License, which permits any non-commercial use, sharing, distribution and reproduction in any medium or format, as long as you give appropriate credit to the original author(s) and the source, provide a link to the Creative Commons licence, and indicate if you modified the licensed material. You do not have permission under this licence to share adapted material derived from this article or parts of it. The images or other third party material in this article are included in the article's Creative Commons licence, unless indicated otherwise in a credit line to the material. If material is not included in the article's Creative Commons licence and your intended use is not permitted by statutory regulation or exceeds the permitted use, you will need to obtain permission directly from the copyright holder. To view a copy of this licence, visit http://creativecommons.org/licenses/by-nc-nd/4.0/.

© The Author(s) 2026